# MSDE

Check for updates

# Enhancing osteogenic differentiation of mesenchymal stem cells seeded on a polycaprolactone/MoS$_2$ nanofibrous scaffold through electrical stimulation

Elahe Amiri,[a] Mehrdad Khakbiz, [iD]*[ab] Behnaz Bakhshandeh, [iD]*[c]
Nika Ranjbar [iD][c] and Javad Mohammadnejad [iD][d]

Recent progress in bone tissue engineering (BTE) has introduced alternative treatments for sizable and non-healing bone defects. Electrical stimulation (ES) has recently been shown to influence bone cells and foster processes such as adhesion, migration, proliferation, and differentiation, which can enhance the bone regeneration process. In this study, we synthesized molybdenum disulfide (MoS$_2$) nanoparticles (NPs) and incorporated them into a polycaprolactone (PCL) polymeric matrix to enhance the electrical conductivity of scaffolds. The PCL/MoS$_2$ nanocomposites were analysed using scanning electron microscopy (SEM), water contact angle measurement, electrical conductivity, and tensile strength assessments. *In vitro* studies evaluated the adhesion of mesenchymal stem cells (MSCs) and the biocompatibility of the fabricated scaffolds using the MTT assay. Biomineral crystal deposition was determined *via in vitro* simulated body fluid (SBF) biomineralization, and alizarin red S assays demonstrated enhanced calcium phosphate deposition on the PCL/MoS$_2$ composite scaffold. Additionally, qPCR analysis revealed that exposing MSCs cultured on PCL/MoS$_2$ to ES for two weeks transcriptionally upregulated osteogenic markers (osteocalcin (OC) and alkaline phosphatase (ALP)) in cells. Using either ES or a differentiation medium alone could enhance osteogenesis. However, when both stimuli were applied concurrently, improved levels of osteogenic markers were observed. Our findings suggest that ES plays a significant role in boosting osteogenic differentiation, particularly when combined with MoS$_2$NPs as an osteogenic enhancer. Therefore, PCL/MoS$_2$ nanofibrous scaffolds can be proposed as suitable candidates for BTE, and ES holds great potential as an effective tool along with commonly used biomaterial scaffolds.

### Design, System, Application

This study enhances bone tissue engineering (BTE) by incorporating MoS$_2$ nanoparticles into a PCL scaffold, aiming to improve electrical conductivity for bone cell behavior. Characterization of scaffold properties is conducted, along with exploring combined electrical stimulation (ES) and MoS$_2$ effects on osteogenic differentiation. The integration of BTE, ES, and nanomaterials is investigated using a PCL/MoS$_2$ scaffold, studying its impact on bone cell behavior and differentiation. The synergistic potential of ES and MoS$_2$ in promoting osteogenic markers is explored, advancing bone regeneration strategies. The study introduces MoS$_2$-enhanced PCL scaffolds, improving electrical conductivity and bone cell interaction. Comprehensive characterization techniques assess the scaffold performance, while MSC experiments demonstrate enhanced adhesion, biocompatibility, and osteogenic differentiation. The study underscores the combined influence of ES and MoS$_2$ on osteogenic markers, emphasizing their role in effective bone regeneration. This research contributes to advancing bone tissue engineering, offering alternatives to traditional autograft treatments.

*[a] Division of Biomedical Engineering, Faculty of New Sciences and Technologies, University of Tehran, Tehran, Iran*
*[b] Department of Chemical and Biochemical Engineering, Rutgers, The State University of New Jersey, Piscataway, NJ, USA.*
*E-mail: Mehrdad.Khakbiz@rutgers.edu*
*[c] Department of Biotechnology, College of Science, University of Tehran, Tehran, Iran. E-mail: b.bakhshandeh@ut.ac.ir*
*[d] Department of Life Science Engineering, Faculty of New Sciences and Technologies, University of Tehran, Tehran, Iran*

## 1. Introduction

Although bone possesses self-regeneration ability, in some cases, such as severe injury and substantial bone loss, difficult and costly treatments are necessary to repair the defect, posing a significant challenge in modern medicine.[1–4] The estimated treatment cost for osteoporosis-related fractures in Europe is projected to rise from 31.7 to 76.7 billion euros by 2050.[5] Previously, autografts have been recognized as the gold standard treatment, despite associated

This journal is © The Royal Society of Chemistry and IChemE 2024

*Mol. Syst. Des. Eng.*, 2024, **9**, 581–596 | 581

problems such as limited tissue supply, infection, immune rejection, and donor-site complications.[6,7] However, bone tissue engineering (BTE) has recently emerged as an alternative method for mimicking autologous bone grafts to restore lost bone volume.[8,9] This approach involves the utilization of scaffolds, stem cells, and growth factors to regulate cell–cell and cell–scaffold interactions, along with the incorporation of signalling stimuli.[10] However, the potential side effects of high doses of bone growth factors and small molecules have raised serious concerns. Accordingly, ES emerges as a promising avenue, showcasing its ability to positively influence bone growth and regeneration. Notably, the application of piezoelectric materials, known for generating electric charges under force, allows bone to regulate tissue growth against external pressure. Consequently, the introduction of piezoelectric scaffolds, with their capacity to generate beneficial electrical charges, stands as a promising approach to promote bone regeneration.[11,12] Previous literature studies underscore the interaction of electrical charges on the surface with functional proteins, creating an extracellular matrix (ECM) layer that facilitates cell deposition and tissue regeneration *via* affecting various signalling pathways, including calcium signalling, TGF-β/BMP, MAPK/ERK, and Wnt/β-catenin.[11,13] Despite decades of exploration into the clinical application of ES for tissue repair, the precise mechanism of action leading to regeneration improvement remains elusive.[14,15] Numerous *in vitro* studies shed light on the tissue regeneration ability of ES, particularly in bone tissue, by influencing a spectrum of stem cell behaviours such as migration, proliferation, differentiation, mineralization, and ECM deposition. The administration of ES occurs in three forms: 1) direct ES involves utilizing non-corrosive conductive electrodes in contact with the culture medium. 2) Capacitive coupling adopts a biologically safe approach, employing a uniform electric field applied to cells on the scaffold by two electrodes at opposite ends. 3) Inductive coupling introduces an electromagnetic field using a conductive coil around the cell culture system, albeit at the cost of time and resources.[16,17] Khaw *et al.* investigated the impact of electrical induction on mesenchymal stem cell (MSC) differentiation by employing a capacitive stimulation method in a bioreactor, adding to our understanding of this innovative approach.[17] The results clearly showed the deposition of calcium and *ALP* in samples exposed to 200 mV mm$^{-1}$ of ES on commercially pure titanium discs.[17] Oftadeh *et al.* assessed the functional synergy between ES and hydroxyapatite NPs for bone differentiation. The results showed that human bone marrow-derived mesenchymal stem cells (BMSCs) cultured on a chitosan/aniline-pentamer/hydroxyapatite scaffold exposed to both stimuli simultaneously expressed higher levels of bone marker genes, such as osteocalcin (*OC*), alkaline phosphatase (*ALP*), osteonectin, and Runx2.[8] Consequently, bone scaffolds should provide a suitable substrate based on the biological, mechanical and electrical properties of the natural tissues.[18,19]

Progress in stem cell technology coupled with developments in tissue engineering has created novel possibilities for bone restoration. Various stem cell types, such as embryonic, adult, and induced pluripotent stem cells, have been recognized for their potential contribution to bone tissue regeneration. MSCs, alternatively termed mesenchymal stromal cells, are multipotent adult stem cells capable of self-renewal and differentiation into multiple cell lineages. This versatility makes MSCs a promising candidate for regenerative medicine. Importantly, BMSCs are valued for their versatility and accessibility in BTE.[20,21] These multipotent cells can differentiate into various cell types, including osteoblasts, which are crucial for bone regeneration. Compared to MSCs from other sources, BMSCs offer a higher proliferation capacity and greater potential for contributing to bone formation.[22] Extensively studied in bone regeneration, their application in clinical settings has yielded promising results. Furthermore, MSCs are considered suitable for allogeneic transplantation because of their immunomodulatory properties, reducing the risk of immune rejection and making allogeneic transplantation a viable therapeutic option.[23,24]

Researchers have employed nanomaterials such as carbon nanotubes and graphene to improve the electrical conductivity of scaffolds.[25,26] Within this category, two-dimensional molybdenum disulfide ($MoS_2$) NPs, recognized for their substantial surface area, favorable electrical conductivity, and reduced toxicity compared to their organic counterparts such as graphene, have been investigated for applications such as photothermal treatment, biosensors, drug delivery, and TE.[27,28] Nazari *et al.* innovatively introduced a nanofiber scaffold composed of $MoS_2$ nanofibers as a conductive element. Nylon nanofibers have been manufactured as mechanical supports and nanotopographic stimuli for cardiac TE. $MoS_2$ nanofibers were synthesized using hydrothermal methods and were incorporated into a nylon solution for electrospinning and exhibited a great improvement in conductivity which could enhance cell adhesion and proliferation and also promote cardiac differentiation and maturation of MSCs without the need for additional biochemical supplements.[29]

In the present study, we introduced $MoS_2$NPs into PCL scaffolds, creating electrospun nanocomposite scaffolds tailored for applications in BTE. Subsequently, we investigated the physicochemical properties of the scaffolds using various methods. The goal of our research was to evaluate the potential improvement in the growth and osteogenic differentiation of human BMSCs seeded on PCL/$MoS_2$ nanofibrous composites by applying ES to enhance the overall effectiveness of BTE strategies.
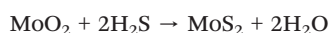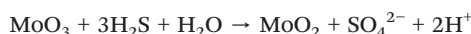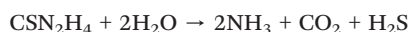
## 2. Materials and methods

### 2.1 Materials

Ammonium heptamolybdate tetrahydrate (($NH_4$)$_6$$Mo_7$$O_{24}$) with a purity of 99.98% (No. 12054-85-2) and thiourea

582 | *Mol. Syst. Des. Eng.*, 2024, **9**, 581–596

This journal is © The Royal Society of Chemistry and IChemE 2024

($CSN_2H_4$) (No. 62-56-6) were purchased from Merck, poly-ε-caprolactone (PCL, No. 440744, average $M_n$ 80 000) and $N,N$-dimethylformamide (DMF, No. 227056) and dichloromethane (DCM, No. 75-09-2) were obtained from Sigma-Aldrich. Also, 3-(4,5-dimethylthiazol-2-yl-2,5-diphenyltetrazolium bromide) (MTT), dimethyl sulfoxide (DMSO) and isopropanol were purchased from Merck (Germany) and used without further purification. Fetal bovine serum (FBS), phosphate buffer saline (PBS), penicillin streptomycin solution, minimum essential medium (MEM) α, and trypsin enzyme were acquired from Gibco (Germany).

## 2.2 MoS$_2$NP synthesis

MoS$_2$NPs were synthesized using a hydrothermal technique. Initially, 0.84 g of ammonium heptamolybdate tetrahydrate and 1.56 g of thiourea were blended with 24 ml of deionized water and vigorously stirred for 6 h. The resultant solution was then transferred to a Teflon-lined stainless steel autoclave and heated to 220 °C for 12 h in an oven. Upon the completion of the reaction, the resulting black powder was gradually cooled to room temperature. Subsequently, it was subjected to three cycles of meticulous washing and centrifugation with a 1:1 ratio of ethanolamine to deionized water. Finally, the black powder was placed in a vacuum oven at 60 °C for 24 h.[30] The essential reaction equations are detailed below:[31]

$$CSN_2H_4 + 2H_2O \rightarrow 2NH_3 + CO_2 + H_2S$$

$$(NH_4)_6Mo7O_{24} \rightarrow 6NH_3 + 7MoO_3 + 3H_2O$$

$$MoO_3 + 3H_2S + H_2O \rightarrow MoO_2 + SO_4^{2-} + 2H^+$$

$$MoO_2 + 2H_2S \rightarrow MoS_2 + 2H_2O$$

## 2.3 Fabrication of the nanofibrous scaffold

Initially, the PCL nanofibrous scaffold was fabricated using electrospinning. This involved dissolving PCL pellets (20% w/v) in DCM/DMF solvent (4:1, v/v) and stirring the solution for 4 h to achieve uniformity.[32] To create the PCL/MoS$_2$ nanofibers, NPs at concentrations of 1%, 2%, and 4% by weight in DMF were subjected to ultrasonic agitation at 300 W for 20 minutes. The agitated NPs were then added to a homogeneous solution of PCL and DCM, followed by stirring. The solution underwent additional sonication to ensure the even dispersion of NPs in the polymer solution. Subsequently, the final solution was transferred to a 3 mL syringe connected to a 22-gauge stainless-steel needle, and a high voltage (DC) of 14 V was applied from the power supply to the needle tip. Throughout the process, a relative humidity level between 26% and 28% at room temperature was maintained. The polymer solution flowed at a steady rate of 1 ml h$^{-1}$, and the distance between the needle tip and the aluminum collector was fixed at 18 cm. The collected mats were vacuum-dried to eliminate any remaining solvent. For further analysis, the samples were cut into suitable dimensions and labeled according to the weight percentage of the NPs (0 wt%, 1 wt%, 2 wt%, and 4 wt%). The surface of the scaffolds was modified through plasma treatment to enhance hydrophilicity for 30 seconds with oxygen level correction, at approximately 0.5 mbar pressure and 60 W power (Zepto, Diener, Ebhausen, Germany).

## 2.4 Scaffold characterization

The morphologies of the PCL/MoS$_2$ nanocomposite and MoS$_2$NPs were analysed using a field emission scanning electron microscope (FESEM) (MIRA3-TESCAN) equipped with an energy dispersive X-ray (EDX) analyser (1.38× NIH USA), to investigate the elemental composition and confirm the presence of the MoS$_2$NPs in the nanocomposite scaffold. Before imaging, samples were coated with gold, and the average fiber diameter was measured using image analysis software (ImageJ, NIH, USA).

X-ray diffraction (XRD) (SIEMENS, D5000) was performed to examine the crystalline nature of the MoS$_2$NPs using an X-ray diffractometer. The pattern was recorded using CuKα radiation as the radiation source, and the diffraction angle 2θ was measured.

Fourier transform infrared (FTIR) spectroscopy (Perkin-Elmer) was conducted over the range of 4000–400 cm$^{-1}$ to investigate the presence of functional groups, the interaction between polymer fibers and NPs, and to determine the incorporation of MoS$_2$ into the scaffold. Additionally, dynamic light scattering (DLS) technology was applied using a HORIBA SZ100 device to study the size distribution and dispersion of MoS$_2$NPs.

**2.4.1 Wettability.** The surface wettability of scaffolds was evaluated *via* water contact angle measurement at room temperature using the dynamic contact angle (AMCAP, version 9.016) with a camera employing a 2× lens and protractor. Initially, 4 μL of deionized water was dispensed onto the mat surface using a micro-syringe attached to a goniometer. Following the release of the droplet from the needle, a sequence of digital images was automatically captured, and these images were subsequently analysed to determine the static contact angle. A minimum of three independent measurements were performed at various locations on the sample, and the mean and the standard deviation were computed.

**2.4.2 Tensile strength.** Tensile strength assessment of nanofibers was carried out through a uniaxial tensile test using the SANTAM stress machine STM20 in Iran. First, samples with a size of 40 × 10 mm$^2$ and a thickness of 10 μm were prepared. The test was performed at room temperature with a speed of 1 mm min$^{-1}$ and a cell load of 200 N, and repeated three times for each sample.

**2.4.3 Conductivity.** The conductivity of the nanocomposites was determined using the standard four-point method with a digital multimeter (three replicates). Eqn (2) was applied to compute the average electrical resistance ($R$). Subsequently, the conductivity ($\sigma$) was

This journal is © The Royal Society of Chemistry and IChemE 2024

*Mol. Syst. Des. Eng.*, 2024, 9, 581–596 | 583

determined by eqn (3), where $L$ represents the length, $A$ denotes the cross-section, and $\rho$ signifies the specific resistance.

$$R = \rho L/A \qquad (1)$$

$$\sigma = L/RA \qquad (2)$$

**2.4.4 Degradation of the PCL/MoS$_2$ nanocomposite scaffold.** To investigate the biodegradation characteristics of the scaffolds, samples were cut and weighed. The initial weight ($W_0$) of each sample was measured, and subsequently, they were immersed in a PBS solution with a pH of 7.4. The samples were placed in a 37 °C incubator for a specified duration. Following the incubation, the samples underwent two rinses with DI water to remove soluble mineral salts and were then dried either in a vacuum or at room temperature. The weight of the dried sample ($W_d$) was measured, and the average percentage of weight loss for each sample was determined using eqn (3).

$$\text{Weightless percentage (\%)} = (W_0 - W_d)/W_0 \times 100 \qquad (3)$$

**2.4.5 Biomineralization assay.** An *in vitro* mineralization test was performed to evaluate the build-up of calcium and inorganic phosphate on the surfaces of nanofibers. First, each sample was cut to a size of 1 cm × 1 cm (three replicates). Mats were then placed in 20 ml SBF (pH = 7.2) within a thermostatic incubator shaker at 37 °C aiming to explore the influence of MoS$_2$NPs on nanofibers. The SBF was prepared according to Kokubo's protocol.[33] Following incubation for 7 and 14 days, the SBF was extracted, and the mats were then rinsed with DI water, and subsequently air-dried at room temperature for SEM and EDX analysis.

**2.4.6 Biocompatibility evaluation.** Before cell seeding, the electrospun scaffolds underwent sterilization through 20 minutes of exposure to ultraviolet (UV) irradiation, followed by immersion in 70% ethanol, and washing with PBS. The scaffolds were then placed at the bottom of tissue culture plate wells, and cells were seeded on samples in alpha-MEM culture media containing FBS (15% v/v) and pen/strep (1 wt% wt/vol). For cell differentiation, media containing 10 mM beta glycerol phosphate, 50 μg ml$^{-1}$ ascorbic acid, and $10^{-7}$ M dexamethasone were used. The plates were maintained in a humidified atmosphere containing 5% CO$_2$ at 37 °C. The culture media were changed every second day.

The morphology of hBMSCs seeded on the scaffolds was analysed using FE-SEM. After sterilization, the scaffolds were placed on a 48-well culture plate, and cells were seeded at a density of 3000 cells per well at passage 3 and incubated in a CO$_2$ incubator at 37 °C. After the incubation for 1 and 3 days, the scaffolds were collected and fixed in 2.5% glutaraldehyde at 4 °C for 3 hours. The scaffolds underwent treatment with gradient ethanol concentrations (50%, 70%, 95%, and 100%) at each concentration. Subsequently, the scaffolds were dried overnight, and images were captured using FE-SEM.

An MTT assay was performed to evaluate the biocompatibility of the nanofibrous scaffolds. The scaffolds were cut into discs to fit a 48-well plate, and cells were seeded at a density of 3000 cells per well at passage 3 and incubated at 37 °C, 5% CO$_2$, and 95% humidity. On days 1, 3, and 7, the culture medium was removed, the cells were washed with PBS, and 100 μL of culture media and 10 μL of 10% MTT solution (5 mg ml$^{-1}$) were added to each well. The plate was incubated in the dark at 37 °C for 3 hours, leading to formazan crystal formation. After discarding the MTT solution, 100 μL DMSO was added to dissolve the purple crystals. After complete dissolution, the scaffolds were removed, and the optical density of the solution was recorded using a spectrophotometer at $\lambda$ = 570 nm. Cell viability was determined by calculating the ratio of the average percent absorbance of the experimental group to that of the control group, which consisted of tissue culture plate (TCP) samples (three replicates).

**2.4.7 Alizarin red S staining.** The detection of calcium precipitates within cells was conducted through alizarin red staining. In this experiment, $10^5$ cells were first seeded at passage 4 on the PCL/2 wt% MoS$_2$ scaffold in a 12-well plate. After 7 and 14 days of incubation, the medium in each well was removed, and the scaffolds, along with the control wells (TCPs), were washed twice with PBS. Subsequently, the cells were fixed in 1% paraformaldehyde for 10 minutes, stained with 2% alizarin red solution (pH 4.2) for 45 minutes at room temperature, and observed under an optical microscope.

## 2.5 Electrical stimulation

After sterilizing the PCL/2 wt% MoS$_2$ scaffold, circle-shaped scaffolds ($A$ = 3.5 cm$^2$) were placed and fixed to the bottom of a custom-built 12-well cell culture plate. The setup was then incubated for 3 hours with culture media. Subsequently, $10^5$ cells at passage 4 were cultured on the PCL/2 wt% MoS$_2$ scaffolds in each well and incubated under ES-free conditions for 24 hours to allow attachment. A bioreactor equipped with two stainless steel electrodes was used for electrical induction. The electrodes underwent sterilization through UV irradiation. Subsequently, the electrodes were brought into contact with the PCL/2 wt% MoS$_2$ scaffold surface in four groups: tissue culture polystyrene (TCP) serving as the control group, scaffold, scaffold with differentiation media (DM), and scaffold with both DM and ES. Waves were generated using a gated electrical pulse generator (GPS, GPS-2105, UK). The current was delivered through two wires connected to the opposing electrodes. Based on the previous literature,[8] the device parameters were configured to a voltage of 2 V, a frequency of 100 Hz, and an induction time of 2 hours per day, which did not demonstrate significant cytotoxicity. While inducing, the tissue culture plates were kept in a 5% CO$_2$ incubator at 37 °C. The culture medium was replaced with fresh media following ES to minimize the potential cytotoxic effect of ES on cells.

**584** | *Mol. Syst. Des. Eng.*, 2024, **9**, 581–596

This journal is © The Royal Society of Chemistry and IChemE 2024

**2.5.1 Transcriptional analyses.** The evaluation of osteogenic marker gene expression after 7 and 14 days was performed quantitatively in cells cultured on the PCL/2 wt% MoS$_2$ scaffold with or without ES. Cells cultured on the TCPs were considered the control group, and each experiment was tested in 3 replicates. RNA was extracted using the phenol–chloroform method with RNX-Plus lysis buffer (Sinaclone, Iran). Cell lysis was collected for 15 min using a 12 000 rpm centrifuge at 4 °C. Subsequently, cDNA was synthesized using a cDNA synthesis kit (Sinaclone, Iran) according to the manufacturer's protocol. The synthesized cDNA was used as a template to evaluate the target genes *via* quantitative real-time polymerase chain reaction (qRT-PCR) using a real-time PCR machine (Rotor-Gene Q, Germany). The hypoxanthine phosphoribosyltransferase 1 (HPRT1) gene was considered the housekeeping gene used for normalization. Table 1 shows the primer sequences used. The RT-PCR reactions were conducted in a reaction of a 2X SYBR Green RT-PCR mix (Amplicon, Denmark), and the qPCR program included an initial step (15 min at 95 °C), followed by 45 cycles (15 s at 95 °C, 20 s at 60 °C, 30 s at 72 °C) and a final extension step (1 min at 72 °C). Melting curve analysis was performed to determine the accuracy of the experiment, and the results were analysed using the comparative $C_t$ method ($2^{-\Delta\Delta CT}$) according to the equation developed by Schmittgen and Livak.[34]

### 2.6 Statistical analysis

Statistical analysis was conducted using the Prism statistical package GraphPad Software, version 8 (San Diego, CA, USA), and the data are expressed as mean ± standard deviation (SD). To determine significance, one-way ANOVA with Tukey's *post hoc* correction test was applied. Statistical significance was established at a threshold of $p < 0.05$, based on three independent experiments, each conducted at least in duplicate.

# 3. Results and discussion

### 3.1 Physicochemical characterization of MoS$_2$NPs

The XRD pattern of MoS$_2$NPs within the range of 0° to 100° is illustrated in Fig. 1d. The diffraction pattern unveiled the single-phase hexagonal crystal structure of the NPs synthesized through the hydrothermal method. Distinct peaks of MoS$_2$NPs appeared at $2\theta$ = 13.96°, 32.95°, 39.61°, and 58.80°, corresponding to the (002), (100), (103), and (110) planes, respectively (JCPDS No. 37-1492).[35] The FE-SEM
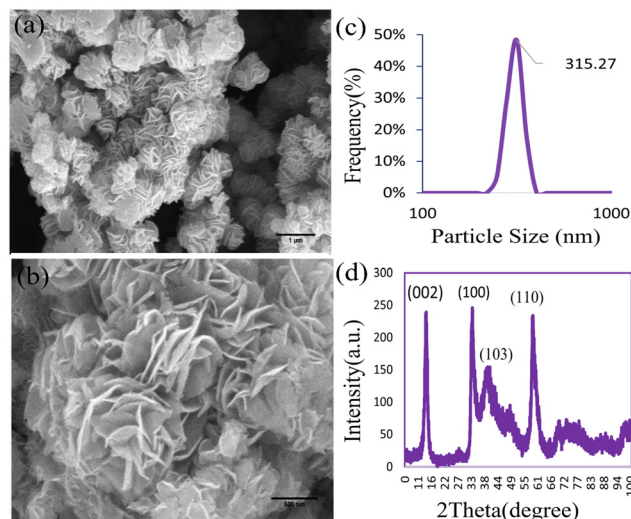


**Fig. 1** (a and b) FE-SEM images of flower-like MoS$_2$NPs prepared by a hydrothermal method at 220 °C for 12 h (scale bar = 1 μm, 500 nm); (c) DLS spectrum of synthesized MoS$_2$NPs showing size distribution and uniformity, (d) XRD pattern of pure MoS$_2$ NPs.

images in Fig. 1a and b depict the morphology of the MoS$_2$-NPs, exhibiting a predominantly thin, fluffy, and slightly curved sheet-like flower structure. The size of the MoS$_2$NPs is approximately 315 nm, as determined through a dynamic light scattering assay (DLS). The DLS particle size distribution plot in Fig. 1c demonstrates a narrow range of nanoflower size distributions, indicating uniformity. The EDX spectrum in Fig. 2d and the elemental mapping images in Fig. 2a–c confirm the homogeneous distribution of elements, including Mo and S, in the nanoflowers.

### 3.2 Physicochemical characterization of PCL/MoS$_2$ scaffolds

FE-SEM images depicting the morphology of PCL and PCL/MoS$_2$ nanofibers with different percentages of NPs are presented in Fig. 3a, c, e and g. A 3D porous network is observed, consisting of nanofibers with uniform sizes and relatively smooth surfaces. The elemental mapping images in Fig. 4 illustrate the incorporation of the MoS$_2$NPs into the polymeric network. The average diameters of PCL, PCL/1 wt% MoS$_2$, PCL/2 wt% MoS$_2$, and PCL/4 wt% MoS$_2$ (Fig. 3b, d, f and h) were estimated to be 248, 259, 304, and 316 nm, respectively. Fig. 5c indicates that the addition of NPs increased the nanofiber diameter, likely due to the high viscosity of the nanofibers after the incorporation NPs.[36] An

**Table 1** Primers used for quantitative RT-PCR

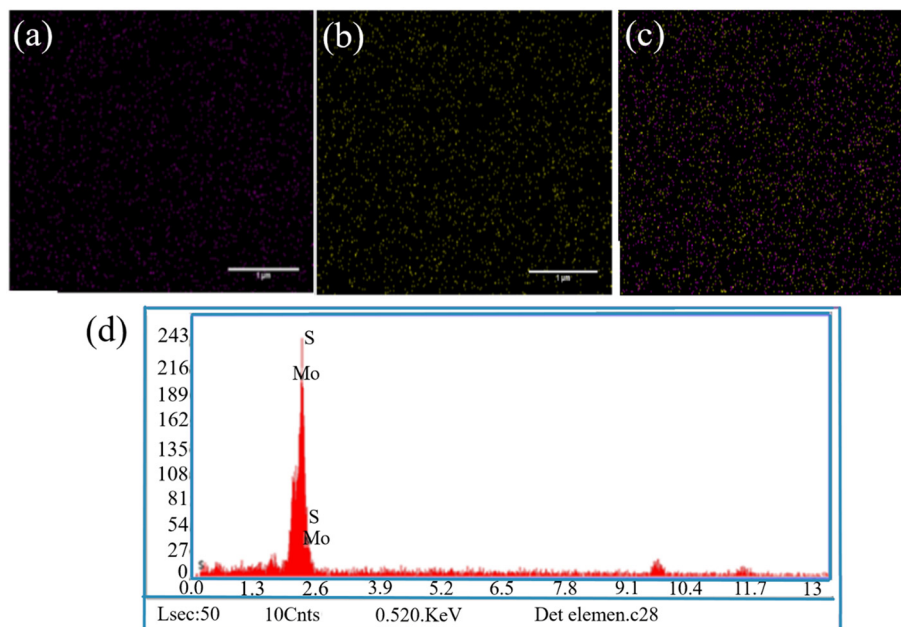| Genes | Primer sequences |
|---|---|
| Alkaline phosphatase (ALP) | TGCAGTACGAGCTGAACAGG (F) |
|  | GTCAATTCTGCCTCCTTCCA (R) |
| Osteocalcin (OC) | GCAGAGTCCAGCAAAGGTG (F) |
|  | CCAGCCATTGATACAGGTAGC (R) |
| Hypoxanthine phosphoribosyltransferase 1 (HPRT1) | CCTGGCGTCGTGATTAGTG (F) |
|  | TCAGTCCTGTCCATAATTAGTCC (R) |

**Fig. 2** (a–c) EDX mapping analysis of elements indicating the existence of Mo and S in NPs; (d) the EDX spectrum of the MoS$_2$ NPs (scale bar = 1 μm).

increase in viscosity correlates with a decline in surface tension, leading to a compromise in the rheological properties of the spinning solution. Consequently, this alteration contributes to the thicker expulsion of the solution jet from the Taylor cone.[37]

Chemical bonds were identified through FTIR spectroscopy. The FTIR spectra of MoS$_2$, PCL, and PCL/MoS$_2$ mats are shown in Fig. 5a. All scaffolds exhibited a strong absorption peak at 1732 cm$^{-1}$, associated with the tensile bands of the carbonyl group. The 2948 and 2868 cm$^{-1}$ peaks represent the symmetric and asymmetric tensile bands of the CH$_2$ group, the 1293 cm$^{-1}$ peak is associated with the C=O and C–C tensile bands, and the 1240 cm$^{-1}$ peak indicates an asymmetric C–O–C stretching band.[27,38] Specific peaks for MoS$_2$ were not detectable in the PCL/MoS$_2$ scaffold spectrum, probably due to the low intensity of the MoS$_2$ peaks or their overlap with the PCL peaks. Nevertheless, a noticeable change in the intensity of the IR spectra in the PCL/MoS$_2$ scaffolds confirms the dispersion of MoS$_2$NPs in the nanofibers and the success of scaffold synthesis.

The introduction of MoS$_2$NPs at a 4% concentration within the nanofiber matrix substantially increased the scaffold conductivity (Fig. 5b). Previous studies have demonstrated that the incorporation of MoS$_2$NPs enhances the conductivity of nylon nanofibers.[29] Given the piezoelectric properties of bone tissue, electroconductive substrates can facilitate the growth and reproduction of bone cells. The utilization of conductive materials in tissue regeneration offers enhanced cell–scaffold interactions, including improved adhesion and proliferation. The scaffold conductivity promotes efficient absorption and deposition of serum proteins, facilitating cell attachment and proliferation. Additionally, the use of conductive biomaterials could
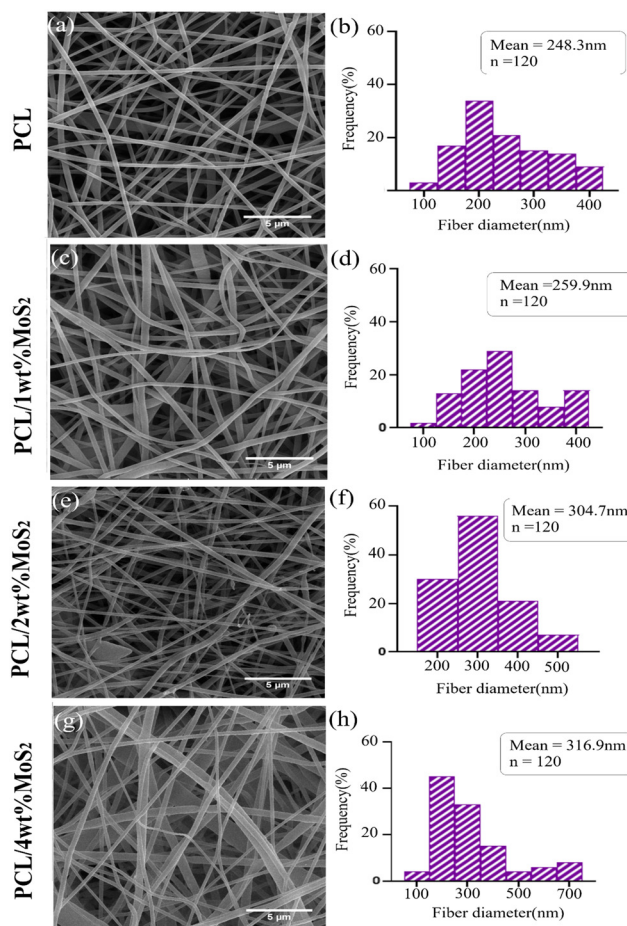


**Fig. 3** FE-SEM images and diameter distribution of nanofibers with different concentrations of MoS$_2$ NPs: (a and b) PCL, (c and d) PCL/1 wt% MoS$_2$, (e and f) PCL/2wt% MoS$_2$, (g and h) PCL/4 wt% MoS$_2$ nanocomposites with uniform size and relatively smooth surface. All data are given as mean ± SD (scale bar = 5 μm).
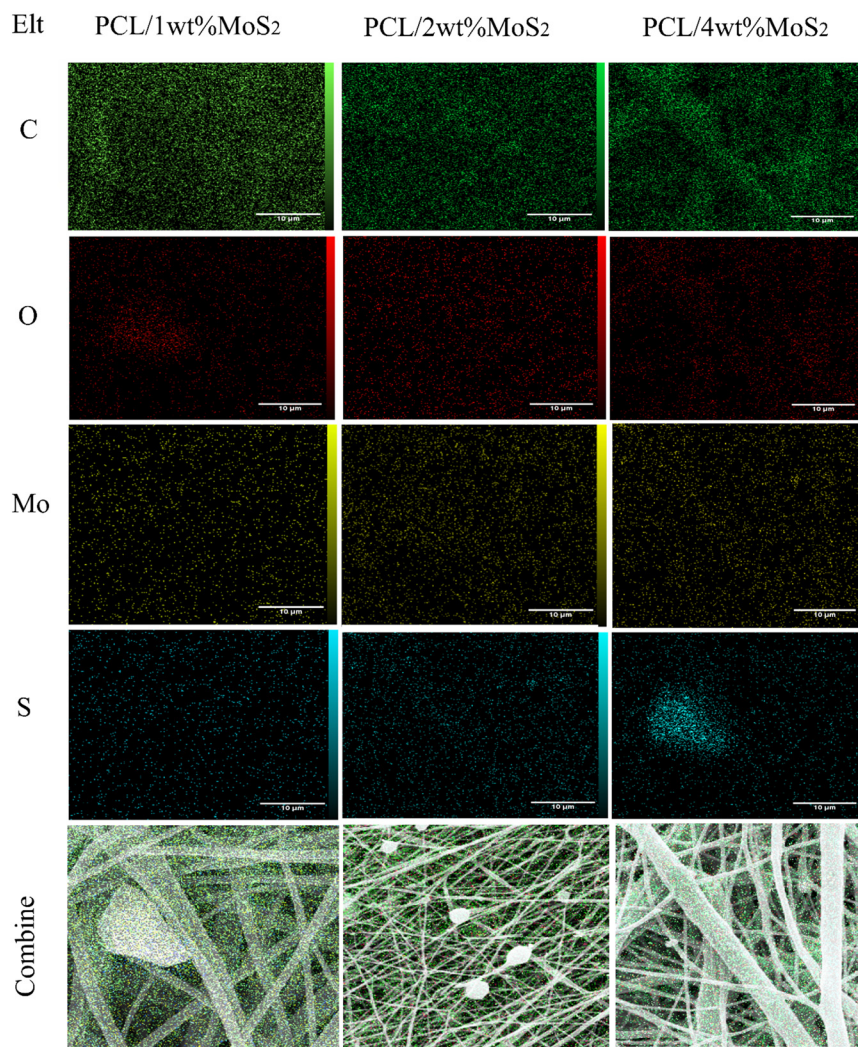
**Fig. 4** EDX map analysis indicating incorporation of MoS$_2$ NPs into PCL networks with different concentrations of NPs (scale bar = 10 μm).

improve the influence of ES on cells, further improving the overall cell–scaffold interactions.[39,40] The potential improvement in current treatment methods for bone defects is evident in a recent study that developed polyvinylidene fluoride (PVDF) and PVDF-polyaniline composite scaffolds equipped with piezoelectricity and conductivity features combined with pulsed electromagnetic field exposure. The results suggested a promising avenue to enhance osteoinductivity, addressing the challenges associated with bone repair.[41]

The hydrophilicity of a scaffold can facilitate the spreading and adherence of bioactive substances, which is beneficial for supporting cellular activities and tissue regeneration.[42]

As indicated in Fig. 5d, the nanofibers exhibited a contact angle exceeding 100° before undergoing plasma treatment, with a minor impact of the added MoS$_2$NPs. Following the plasma modification, there was a significant decrease in the hydrophobicity of the nanocomposites, approaching approximately 10°. This treatment can induce

dehydrogenation, radical formation, and surface roughening, while also enhancing the hydrophilic properties by introducing carboxyl and amide groups on the fiber surface.[27]

A scaffold plays a pivotal role in offering essential mechanical support during the initial phases of new bone growth, and its mechanical function is crucial for effective bone repair. The tensile characteristics of the scaffolds were evaluated, and the findings are depicted in Fig. 6a. The introduction of MoS$_2$ into PCL scaffolds significantly decreased the mechanical properties, with a threefold reduction observed in PCL/4 wt% MoS$_2$ compared to pure PCL scaffolds. However, PCL/2 wt% MoS$_2$ exhibited the highest tensile strength and mechanical properties when compared to PCL scaffolds with 1 wt% and 2 wt% MoS$_2$ (Fig. 6b). The fracture strain of the PCL nanofibers surpassed the 420% threshold, while across all PCL/MoS$_2$ nanocomposites, the fracture strain consistently remained below 150%. These results align with previous research demonstrating a decrease in the fracture strain of a nanocomposite with 1.5% MoS$_2$NPs compared to pure PCL.[43] The diminishing mechanical properties are attributed to the

This journal is © The Royal Society of Chemistry and IChemE 2024

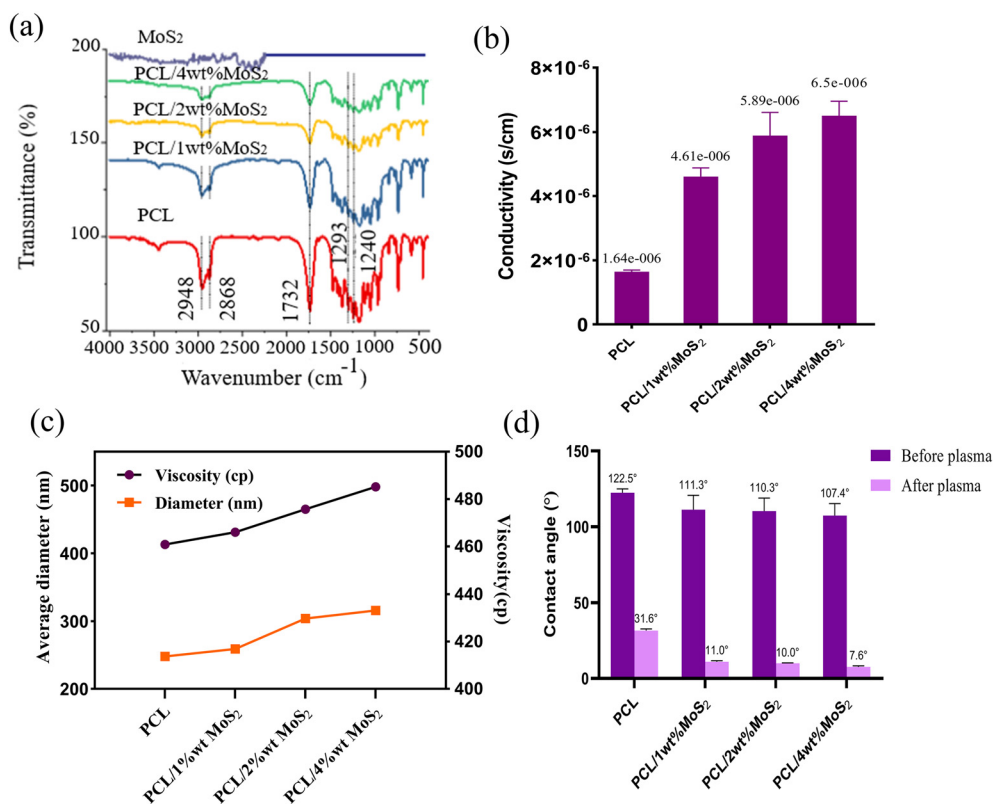*Mol. Syst. Des. Eng.*, 2024, **9**, 581–596 | **587**

**Fig. 5** (a) FTIR spectra of PCL/MoS$_2$ nanofibers compared with PCL. (b) The volume conductivity diagram of PCL/MoS$_2$ nanofibers showing a significant increase. (c) Effect of dynamic viscosity on electrospun nanofibers containing various amounts of MoS$_2$NPs. (d) Decrease in contact angles of nanofibers after plasma treatment. All data are given as mean ± SD.
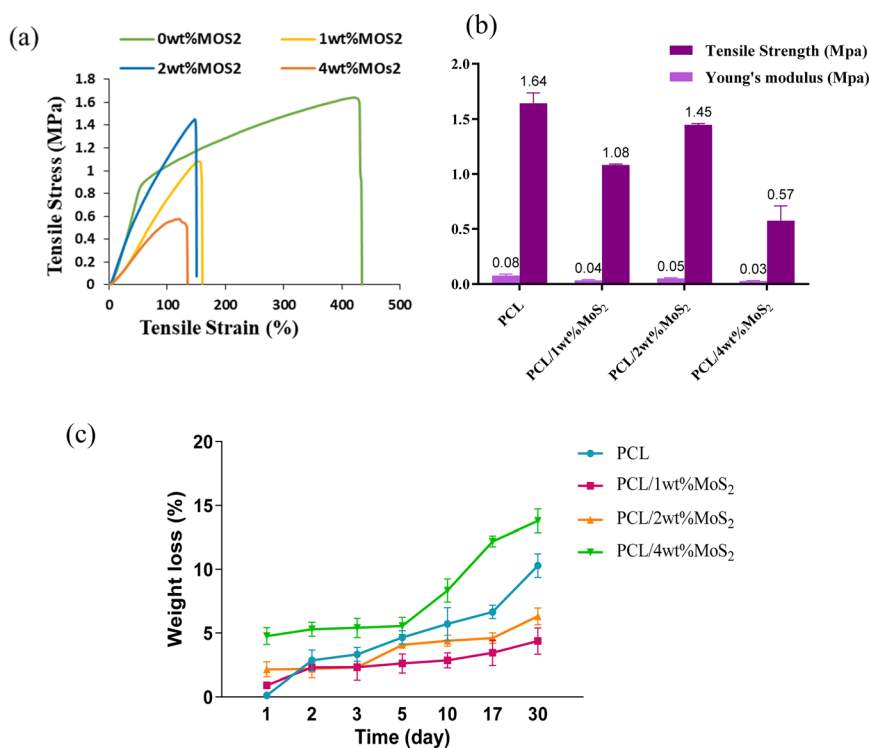


**Fig. 6** Physical characterization of the PCL/MoS$_2$ scaffolds compared to the PCL scaffold. (a) The mechanical properties of electrospun nanofiber scaffolds are shown by tensile stress–strain curves. (b) Comparison of tensile strength and calculated Young's modulus of scaffolds and reducing effect of NPs on the mechanical properties of scaffolds. (c) Degradation characterization of the scaffolds. Values are given as mean ± standard deviation.

**588** | *Mol. Syst. Des. Eng.*, 2024, **9**, 581–596

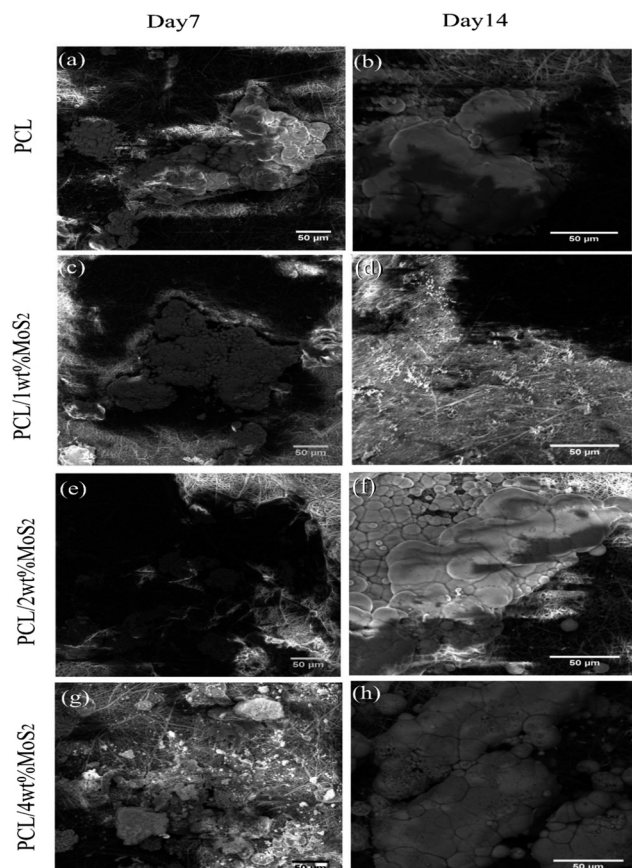This journal is © The Royal Society of Chemistry and IChemE 2024

**Fig. 7** SEM micrographs of electrospun scaffolds after biomineralization in SBF for 7 and 14 days. (a and b) PCL, (c and d) PCL/1 wt% MoS₂, (e and f) PCL/2 wt% MoS₂, and (g and h) PCL/4 wt% MoS₂ (scale bar = 50 μm).

potential misalignment of polymer molecules, especially in the presence of NPs.[27] Thus, to overcome the limited mechanical properties of PCL/MoS$_2$ nanocomposites, it is essential to introduce supplementary components into their structure.

Fig. 6c illustrates the changes in mass loss observed in the PCL/MoS$_2$ scaffold after one month of immersion in PBS. The degradation of pure PCL was measured at around 10.29%, whereas for nanocomposites containing 1% and 2% MoS$_2$, the degradation was below 6%. This aligns with a previous study, demonstrating that the addition of MoS$_2$NPs up to 1 wt% in PCL did not lead to any noticeable alteration in weight loss.[43] The weight loss remained consistently

gradual across all scaffolds, slightly accelerating in PCL/4 wt% MoS$_2$, likely due to the larger diameter and increased porosity of the fibers.[44] During the initial phases of degradation, the scaffold demonstrated a slow weight loss. After 10 days, the degradation rate decreased, and the curve shifted towards rapid degradation.

The *in vitro* mineralization of PCL/MoS$_2$ scaffolds was investigated using a simulated body fluid solution. The SEM images in Fig. 7a–h depict the mineralization of PCL/MoS$_2$ scaffolds after 7 and 14 days of treatment with the SBF solution. The PCL scaffold exhibited the formation of mineral aggregates, consistent with a previous report.[45] Due to the hydrolytic degradation of PCL, carboxylic (–COOH) and hydroxylic (–OH) functional groups were released through the cleavage of ester linkages on the PCL surfaces. Thus, PCL can be regarded as a bioactive biomaterial since these negatively charged groups attract positively charged calcium ions, resulting in their precipitation on the fiber surface as hydroxyapatite crystals.[46]

A microanalysis report indicated an increase in the Ca$^{2+}$ content of the scaffolds over time, as presented in Table 2. The introduction of MoS$_2$ into the PCL fibers resulted in an augmentation of mineral deposition on the surfaces of the nanocomposite scaffold. This observation aligns with a previous study that noted enhanced mineralization in PCL/zein/MoS$_2$ compared to PCL/zein, attributed to the negative surface charge on MoS$_2$ (ref. 47). In our investigation, the precipitation weight percentage ratio of Ca$^{2+}$/P on the PCL scaffold after 14 days of incubation was 1.31, while the PCL/4 wt% MoS$_2$ scaffold exhibited a slightly higher ratio at 1.42. This difference in ratios indicates the impact of MoS$_2$ incorporation on biomineralization. The incorporation of MoS$_2$ in the nanofibrous scaffolds leverages their expansive surface area and promotes effective nucleation with inorganic mineral ions in the SBF solution.[47] This enhanced mineral ion nucleation consistently supports the growth of hydroxyapatite, facilitating osteoconductive regulation. Consequently, these materials hold promise as biocompatible substrates that can encourage the proliferation of hBMSCs.

Applying an advanced multi-scale model, we assessed the mechanical characteristics of the scaffolds. The pivotal role of Digimat 2017.0 in facilitating the development of a precisely tailored micromechanical model cannot be overstated. This model intricately incorporates the representation of volume elements, commonly known as the

**Table 2** The presence of Ca$^{2+}$ and P on the scaffold surface respectively in EDX results after 14 days of incubation in SBF

| PCL | | | PCL/1 wt% MoS₂ | | | PCL/2 wt% MoS₂ | | | PCL/4 wt% MoS₂ | | |
|---|---|---|---|---|---|---|---|---|---|---|---|
| Element | Weight% | Atomic% | Element | Weight% | Atomic% | Element | Weight% | Atomic% | Element | Weight% | Atomic% |
| Na | 4.11 | 6.08 | Na | 4.11 | 5.01 | Na | 3.24 | 4.79 | Na | 3.83 | 5.70 |
| Mg | 4.81 | 6.73 | Mg | 4.73 | 6.69 | Mg | 5.41 | 7.58 | Mg | 4.70 | 6.62 |
| P | 36.48 | 40.03 | P | 37.13 | 39.76 | P | 36.14 | 39.73 | P | 35.82 | 39.56 |
| S | 2.29 | 2.43 | S | 2.03 | 3.34 | S | 3.45 | 3.66 | S | 1.72 | 1.83 |
| Cl | 3.27 | 3.14 | Cl | 1.39 | 2.68 | Cl | 2.17 | 2.09 | Cl | 2.21 | 2.13 |
| K | 0.93 | 0.81 | K | 0.85 | 0.34 | K | 0.84 | 0.73 | K | 0.64 | 0.56 |
| Ca | 48.10 | 40.79 | Ca | 49.76 | 42.18 | Ca | 48.75 | 41.42 | Ca | 51.08 | 43.59 |
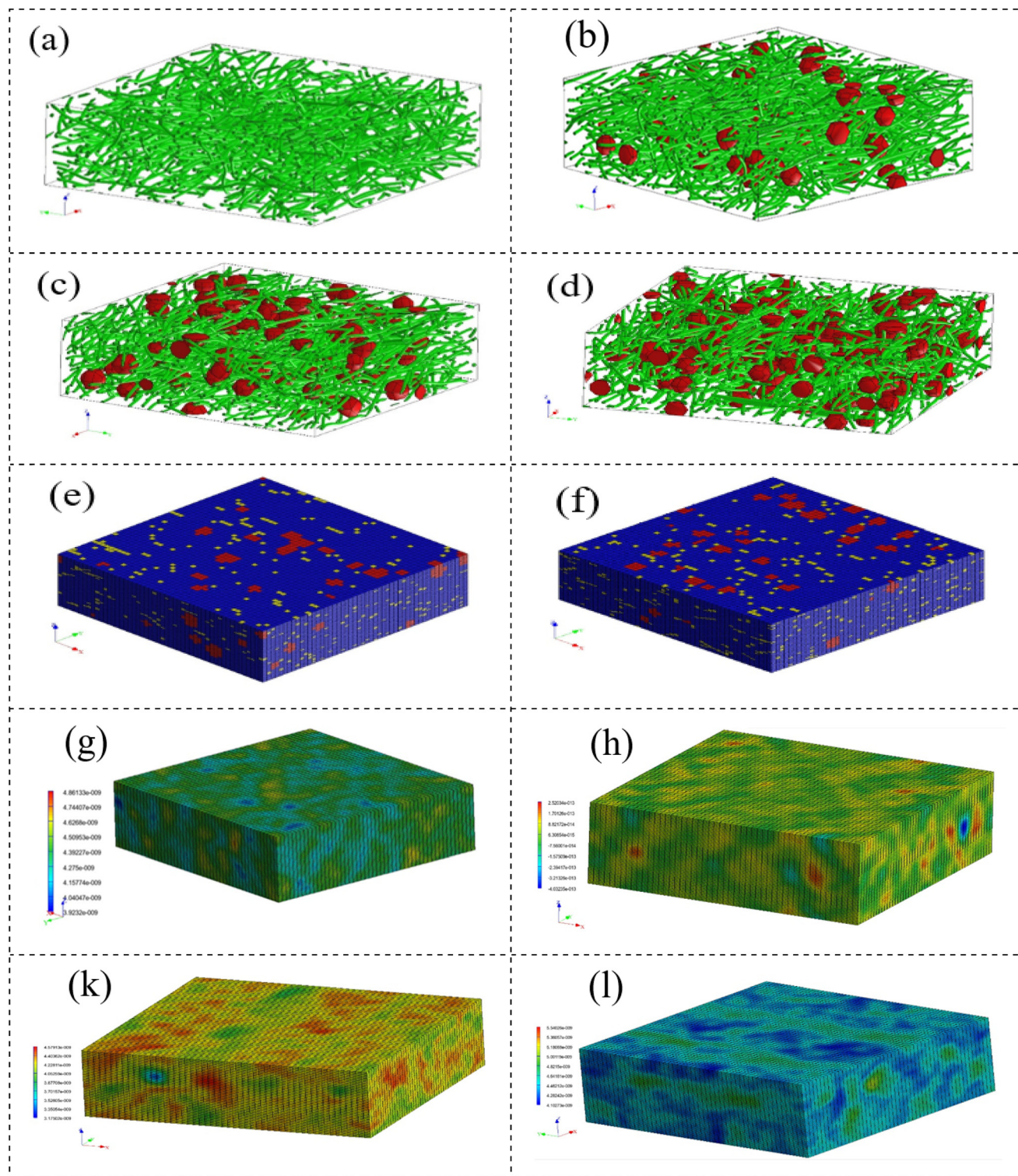
**Fig. 8** (a–d) RVE models for different scaffolds. (e and f) Mesh models for 2% and 4% MoS$_2$ samples. (g, h, k and l) Stress distribution for samples.

representative volume element (RVE). Importantly, the current model sharply focuses on the RVE strategically positioned close to the fibers. This strategic methodological approach was systematically implemented in the comprehensive examination of composite scaffolds, ensuring a homogeneous strain distribution across both the

reinforcement and matrix phases.[48] Initiating the simulation involved a comprehensive selection process to determine the 3D geometric configuration of the scaffolds. Leveraging the advanced capabilities of the Digimat FE module, we precisely created the intricate geometries of the MoS$_2$ reinforcements. Subsequently, the model underwent a

**590** | *Mol. Syst. Des. Eng.*, 2024, **9**, 581–596

This journal is © The Royal Society of Chemistry and IChemE 2024

detailed loading process in Digimat-MF, aligned with its designated loading objectives. The detailed presentation in Fig. 8a–h visually illustrates the three-dimensional shapes of the representative volume elements (RVEs) for both the scaffolds and scaffold composites. The systematic construction of the finite element mesh model, employing quadrilateral elements, unfolded seamlessly through a complementary technique, adhering to a global approximate size constraint of 2 nm.

Fig. 9 illustrates the stress and strain distribution in the specimens. The introduction of NPs resulted in a noticeable concentration of stress, reaching seven times higher than the matrix stress in the 2% nanoparticle sample and five times higher in the 4% nanoparticle sample. Moreover, the extent of the stress concentration region increased when the nanoparticles were in closer proximity to each other. These findings highlight that, in the case of agglomeration, a localized area of stress concentration emerges, contributing to a decrease in the mechanical strength of the scaffolds. The findings suggest that an increase in $MoS_2$ nanoparticles resulted in higher maximum stress (Fig. 8e, h, k and l), simultaneously revealing a reduction in maximum strain. Fig. 8 illustrates that the polymer background undergoes the most substantial strain, whereas the nanoparticles display a strain closer to zero.

The predicted stress–strain plot of the nanocomposite is displayed in Fig. 9, indicating that the samples exhibit elastoplastic behaviour. A significant enhancement in the mechanical properties of the scaffold was observed with an increase in the $MoS_2$ content. An increase in $MoS_2$ content from 1% to 4% wt increases strength by 33%. The composite scaffolds were reinforced with $MoS_2$ through several mechanisms, including the bridging of $MoS_2$ between the initiated cracks in the matrix, effectively preventing crack growth. Additionally, the presence of nanoparticles leads to crack deflection during growth. Finally, pulling out the nanoparticles reduces the applied force. By comparing the predicted data with the experimental results, it can be inferred that the model accurately predicts the mechanical properties of the composite material with an accuracy of 83%.
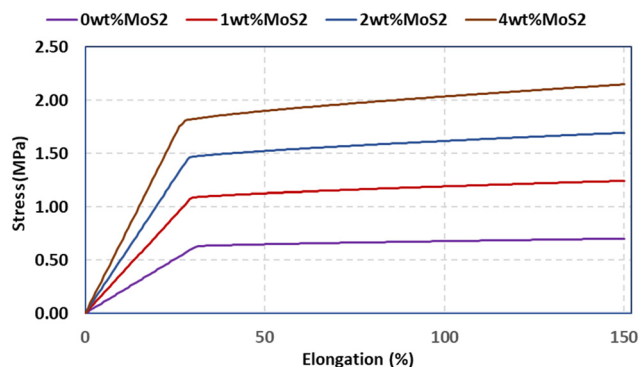
## 3.3 Biological studies

### 3.3.1 Biocompatibility of PCL/MoS₂ scaffolds.
Cell viability and proliferation, and adhesion to biomaterials represent critical factors in TE applications. The surface properties and structure emerge as the primary determinants regulating cell behaviour and growth.[49] Thus, an MTT assay was conducted to evaluate the biological performance of the scaffolds and their impact on growth and viability.

Fig. 10a, c, e and g illustrate the favorable adhesion of hBMSCs on the scaffolds after 24 hours, attributed to the wettability of the scaffold. Subsequently, the cells spread over the fibers (Fig. 10b, d, f and h). Using high-magnification SEM images (Fig. 10a and b), it was observed that the PCL scaffold surface exhibited fewer irregularities compared to the PCL/MoS₂ scaffolds. As a result, the cell adhesion on the PCL scaffold decreased in comparison with the other scaffolds. In a related study, it was found that hMSCs seeded on rough PCL fibers displayed a spreading morphology,
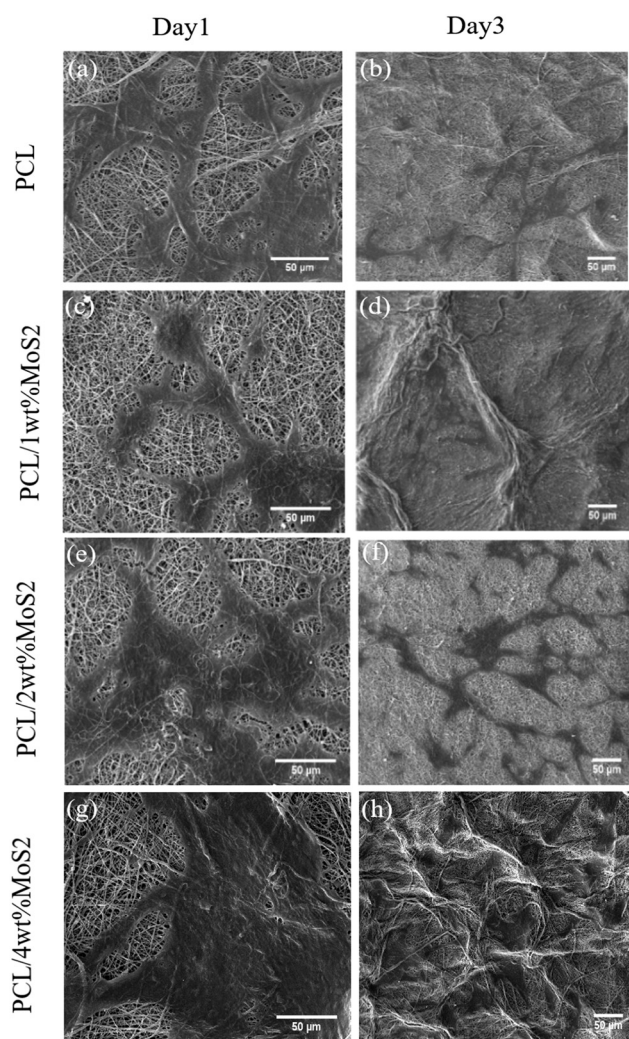


**Fig. 10** (a) SEM images of adhesion of MSCs on scaffolds for 1 and 3 days. (a and b) PCL, (c and d) PCL/1 wt% MoS₂, (e and f) PCL/2 wt% MoS₂, and (g and h) PCL/4 wt% MoS₂ (scale bar = 50 μm).



**Fig. 9** Stress–strain curves for different samples.

indicative of robust attachment. Conversely, cells seeded on smoother fibers exhibited signs of poor adhesion. This discrepancy was attributed to rougher fiber surfaces providing more anchor sites for cell adhesion compared to smoother surfaces.[50] The topological features of the scaffold surface, including wettability and roughness, play a crucial role in cell migration by impacting on the ECM protein and serum component adsorption, along with hBMSC proteins.[29] As a result, robust cell adhesion supports enhanced proliferation on the scaffold, leading to bone cell formation and damage.[51]

The initial cell adhesion within the first 24 hours has a significant impact on proliferation through integrin-mediated signalling. In contrast, inadequate cell viability or adhesion can lead to apoptosis, impeding cell proliferation.[51] The potential cytotoxicity of the scaffolds was assessed using the MTT assay after 1, 3, and 7 days. As shown in Fig. 11, the cell viability on the first day was almost similar among all nanocomposite scaffolds, slightly surpassing that of the PCL scaffolds. Subsequently, at days 3 and 7, the cell viability exceeded 85% for all tested PCL/MoS$_2$ scaffolds, with the highest observed viability found in the nanocomposite containing 2 wt% MoS$_2$NPs. These results indicate that the MoS$_2$NPs could sufficiently preserve cell viability and do not have a significant cytotoxic effect on cells, as confirmed by a study revealing that incorporating exfoliated MoS$_2$ nanosheets into PCL/zein composite nanofibers enhances biocompatibility and cell proliferation.[47] Overall, the PCL/MoS$_2$ scaffolds serve as biocompatible platforms, actively encouraging cell proliferation and supporting strong cell adhesion.

**3.3.2 Biomineralization assay (alizarin red staining).** Alizarin red S staining was conducted to examine the mineral deposits on PCL/2 wt% MoS$_2$ on days 7 and 14. In Fig. 12a and c, red spots on the scaffold surface indicate mineral deposits within the pores. In contrast, the strains on the control sample (bottom of the well) were more uniformly

scattered and clustered in shape (Fig. 12b and d). The scaffold exhibited a higher mineral content compared to the control, attributed to its microporous nature providing an expanded surface area for cell adhesion and facilitating cell aggregation within the pores. This phenomenon aligns with studies suggesting that densely populated osteoprogenitors enhance mineral deposition, especially when osteoporotic cells form dense clusters.[52] A study revealed a notable increase in mineralization, as evidenced by alizarin red staining, in BMSCs cultured on PCL scaffolds.[53] A parallel investigation involving BMSCs cultured on PCL/1% MoS$_2$ groups exhibited noticeable mineral deposits compared to the PCL group, with increasing deposits on the fiber membranes.[43] Furthermore, another study highlighted the osteogenic potential of albumin-induced exfoliated conductive MoS$_2$ nanosheets, showing early differentiation of pre-osteoblast MC3T3-E1 compared to pristine PCL/zein.[27] These examples collectively emphasize the significance of MoS$_2$ incorporation in promoting mineralization and osteogenic differentiation, supporting the potential application of MoS$_2$ scaffolds in BTE.

**3.3.3 Osteogenic gene expression analysis.** The concept that focal changes in mechanical and electrical inducers can influence various biological processes has been firmly established. Electric energy plays a critical role in several processes, including membrane permeability, cell signalling, cell proliferation, and ECM organization.[54] The positive effect of ES combined with other induction factors on osteogenesis has been investigated in numerous *in vitro* and *in vivo* BTE studies. This combination significantly affects the proliferation and differentiation of MSCs, ultimately leading to new bone formation.[55] In a previous study, the influence
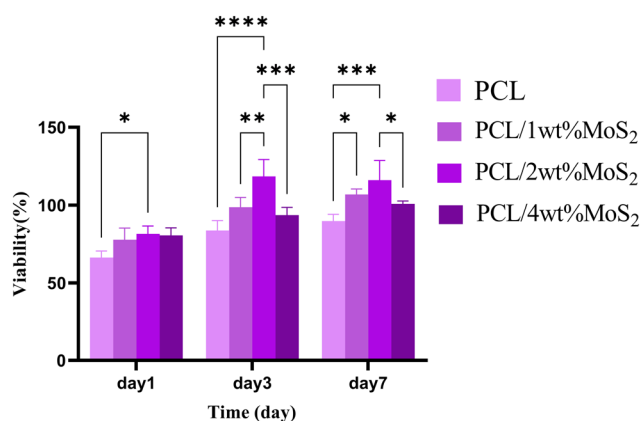


Fig. 11 *In vitro* cellular response; MTT results of scaffolds on MSC cell viability. Values are presented as mean ± SD of three different experiments. *: $P < 0.05$; **: $P < 0.005$; ***; ****: $P < 0.0005$. All scaffolds excluding MoS$_2$ performed suitable biological responses compared with the control group.
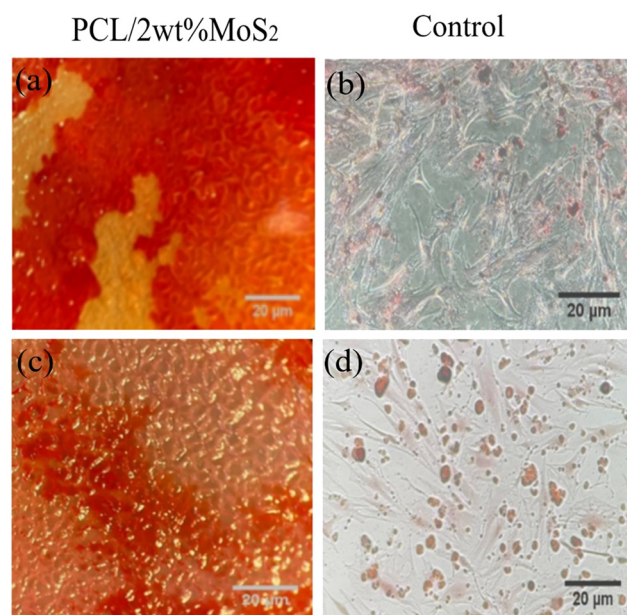


Fig. 12 Alizarin red staining of BMSCs cultured on PCL/2 wt% MoS$_2$ scaffolds and tissue culture plates (TCPs) after 7 days (a and b) and 14 days (c and d). The scale bar represents 20 μm.

of two distinct electric field regimes for 7 days on osteogenic differentiation was explored. The disrupted (4/4) regime was found to be associated with the BMP/Smad4 pathways, leading to an upregulation of Runx2/OCN gene expression on day 7, while exerting a relatively minor impact on ALP activity. In contrast, the consecutive (12/12) regime activated the canonical Wnt/β-catenin signaling pathway through mechanotransduction cues, resulting in a significant elevation of ALP activity and Sp7 gene expression on day 7.[56]

Moreover, ES promotes bone healing by stimulating the calcium–calmodulin pathway, which occurs through the upregulation of bone morphogenetic proteins, TGF-β, and other cytokines.[57] Considering that cell adhesion, proliferation, and differentiation involve multifactorial mechanisms influenced by various biochemical and biophysical stimuli, studies emphasize the importance of synergistic effects between different stimulators which may lead to more efficient TE differentiation protocols.[58] The findings of a study revealed that the unique surface characteristics of poly-L-lysine (PLL)-poly(lactic-co-glycolic acid) (PLGA)/graphene oxide (GO) (PLL-PLGA/GO) hybrid fiber matrices facilitate protein adsorption and effectively inhibit pathogen proliferation. Furthermore, the matrices demonstrate an enhanced regulatory impact on MC3T3-E1 cell behaviors under ES, improving cell proliferation, differentiation, adhesion, ALP activity, calcium deposition, and expression of osteogenesis-related genes.[59]

In this study, we explored the synergistic effects of hormones (beta-glycerol phosphate, ascorbic acid, and dexamethasone) and ES on the osteogenic differentiation of hBMSCs seeded on a PCL/2 wt% MoS$_2$ scaffold. The expression of osteogenesis-related genes, including ALP and OC, at 7 and 14 days was quantitatively analyzed using qRT-PCR. According to the findings illustrated in Fig. 13a and b, the transcriptional activity of both osteogenic markers increased in cells seeded on PCL/2 wt% MoS$_2$ embedded scaffolds compared to tissue culture polystyrene (TCPS). ALP

and OC activities in cells cultured on PCL/2 wt% MoS$_2$ without electrical and hormonal stimulation were not significantly different from those in cells cultured on TCPS. Osteogenesis, however, was enhanced when differentiation media were used separately. On the 14th day of culture, the presence of both ES and differentiation media resulted in a significant increase in marker expression. Specifically, the expression of ALP markers approximately doubled, while the expression of OC markers increased by 1.5 times, compared to the scaffold that did not receive ES.

## 4. Conclusion

In this study, PCL/MoS$_2$ nanofiber scaffolds were successfully fabricated using electrospinning. The physicochemical and biological characteristics of the scaffolds were evaluated, revealing the proper incorporation of MoS$_2$NPs into the PCL composites. Despite the absence of a positive effect on the mechanical strength with increasing MoS$_2$ content, the composite PCL/MoS$_2$ scaffolds demonstrated enhanced biomineral deposition on their surfaces. Furthermore, the MTT assay suggested increased biocompatibility and improved cell adhesion of the PCL/MoS$_2$ scaffolds. These findings suggest that the PCL/MoS$_2$ scaffolds are promising materials for BTE applications. Moreover, significant cell differentiation on these scaffolds was observed using qRT-PCR. The influence of prolonged ES combined with exposure to differentiation media revealed substantial upregulation of ALP and OC transcription on days 7 and 14 in all test groups, regardless of ES. The transcript levels of bone markers were notably lower in the TCPS group than in the other groups, while the combined effect of differentiation media and ES significantly upregulated OC and ALP compared to TCPS.

In conclusion, the simultaneous application of differentiation media and ES further enhanced osteogenesis, potentially owing to their sequential intervention in the mineralization and osteogenic signaling pathways. This study suggests that exploring the functional synergy between different stimulators and optimizing their interactions may lead to the development of more effective therapeutic tools for bone regeneration. However, it is essential to acknowledge the limitations of the present study. This investigation primarily focused on in vitro assessments, and further immunocytochemistry assays and in vivo studies are required to validate the effectiveness of PCL/MoS$_2$ scaffolds in real physiological environments. Additionally, long-term effects and potential adverse reactions need to be thoroughly evaluated before clinical translation. Future research should address these limitations and explore innovative strategies for optimizing the scaffold performance and promoting successful clinical applications.
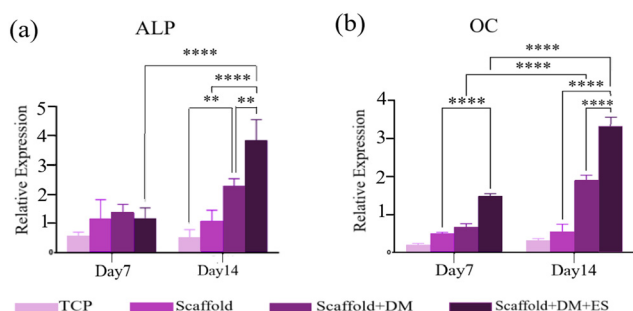


Fig. 13 Impact of ES on the upregulation of gene transcription levels of alkaline phosphatase (ALP) (a) and osteocalcin (OC) (b) in cells seeded on PCL/2 wt% MoS$_2$ scaffolds after 7 and 14 days. The experimental groups include TCP (tissue culture plate), scaffold, scaffold + differentiation media (DM), and scaffold + DM + electrical stimulation (ES). Data represent the mean ± SD of three replicate experiments. Statistical significance is indicated as ** for $P < 0.005$ and **** for $P < 0.0005$.

## Abbreviations

| | |
|---|---|
| TE | Tissue engineering |
| BTE | Bone tissue engineering |
| ECM | Extracellular matrix |

This journal is © The Royal Society of Chemistry and IChemE 2024

Mol. Syst. Des. Eng., 2024, 9, 581–596 | 593

| PCL | Polycaprolactone |
| MoS$_2$NPs | Molybdenum disulfide nanoparticles |
| SEM | Scanning electron microscopy |
| MSCs | Mesenchymal stem cells |
| ES | Electrical stimulation |
| DCM | Dichloromethane |
| DMF | Dimethylformamide |
| EDX | Energy dispersive X-ray |
| FE-SEM | Field emission scanning electron microscopy |
| XRD | X-ray diffraction |
| FTIR | Fourier transform infrared |
| DLS | Dynamic light scattering |
| TCP | Tissue culture polystyrene |
| ALP | Alkaline phosphatase |
| OC | Osteocalcin |
| HPRT1 | Hypoxanthine phosphoribosyltransferase 1 |

## Funding

## Author contributions

E. A.: conceptualization; investigation; methodology; data analysis; visualization. M. Kh. and B. B.: conceptualization; review and editing; supervision; project administration; funding acquisition. N. R.: methodology; data curation; review and editing. J. M.: co-supervision. All authors have read and agreed to the published version of the manuscript.

## Conflicts of interest

There are no conflicts to declare.

## References

1 L. Leppik, K. M. C. Oliveira, M. B. Bhavsar and J. H. Barker, Electrical stimulation in bone tissue engineering treatments, *Eur. J. Trauma Emerg. Surg.*, 2020, **46**(2), 231–244.

2 G. Zhu, T. Zhang, M. Chen, K. Yao, X. Huang and B. Zhang, *et al.*, Bone physiological microenvironment and healing mechanism: Basis for future bone-tissue engineering scaffolds, *Bioact. Mater.*, 2021, **6**(11), 4110–4140.

3 S. Jafarkhani, E. Amiri, S. Moazzeni, T. Zohoorian-Abootorabi, M. Eftekhary and S. Aminnezhad, *et al.*, Exploring the Effects of Micro-Nano Surface Topography on MG63 Osteoblast-Like Cell Responses: An In Vitro Study, *Colloids Surf., A*, 2023, 131872.

4 T. Zohoorian-Abootorabi, A. A. Meratan, S. Jafarkhani, V. Muronetz, T. Haertlé and A. A. Saboury, Modulation of cytotoxic amyloid fibrillation and mitochondrial damage of α-synuclein by catechols mediated conformational changes, *Sci. Rep.*, 2023, **13**(1), 5275.

5 W. Wang, J. R. P. Junior, P. R. L. Nalesso, D. Musson, J. Cornish and F. Mendonca, *et al.*, Engineered 3D printed poly(varepsilon-caprolactone)/graphene scaffolds for bone tissue engineering, *Mater. Sci. Eng., C*, 2019, **100**, 759–770.

6 S. Jafarkhani, M. Khakbiz, G. Amoabediny, J. Mohammadi, M. Tahmasebipour and H. Rabbani, *et al.*, A novel co-culture assay to evaluate the effects of sympathetic innervation on vascular smooth muscle differentiation, *Bioorg. Chem.*, 2023, **133**, 106233.

7 E. Amiri, P. Sanjarnia, B. Sadri, S. Jafarkhani and M. Khakbiz, Recent advances and future directions of 3D to 6D printing in brain cancer treatment and neural tissue engineering, *Biomed. Mater.*, 2023, 33–48.

8 M. O. Oftadeh, B. Bakhshandeh, M. M. Dehghan and A. Khojasteh, Sequential application of mineralized electroconductive scaffold and electrical stimulation for efficient osteogenesis, *J. Biomed. Mater. Res., Part A*, 2018, **106**(5), 1200–1210.

9 M. Sadeghi, B. Bakhshandeh, M. M. Dehghan, M. R. Mehrnia and A. Khojasteh, Functional synergy of anti-mir221 and nanohydroxyapatite scaffold in bone tissue engineering of rat skull, *J. Mater. Sci.: Mater. Med.*, 2016, **27**(8), 132.

10 B. Bakhshandeh, P. Zarrintaj, M. O. Oftadeh, F. Keramati, H. Fouladiha and S. Sohrabi-Jahromi, *et al.*, Tissue engineering; strategies, tissues, and biomaterials, *Biotechnol. Genet. Eng. Rev.*, 2017, **33**(2), 144–172.

11 R. Das, E. J. Curry, T. T. Le, G. Awale, Y. Liu and S. Li, *et al.*, Biodegradable nanofiber bone-tissue scaffold as remotely-controlled and self-powering electrical stimulator, *Nano Energy*, 2020, **76**, 105028.

12 D. Khare, B. Basu and A. K. Dubey, Electrical stimulation and piezoelectric biomaterials for bone tissue engineering applications, *Biomaterials*, 2020, **258**, 120280.

13 B. Bakhshandeh, N. Ranjbar, A. Abbasi, E. Amiri, A. Abedi and M. R. Mehrabi, *et al.*, Recent Progress in the Manipulation of Biochemical and Biophysical Cues for Engineering Functional Tissues, *Bioeng. Transl. Med.*, 2022, e10383.

14 A. Babaie, B. Bakhshandeh, A. Abedi, J. Mohammadnejad, I. Shabani and A. Ardeshirylajimi, *et al.*, Synergistic effects of conductive PVA/PEDOT electrospun scaffolds and electrical stimulation for more effective neural tissue engineering, *Eur. Polym. J.*, 2020, **140**, 110051.

15 N. Ranjbar, B. Bakhshandeh and C. P. Pennisi, Electroconductive Nanofibrous Scaffolds Enable Neuronal Differentiation in Response to Electrical Stimulation without Exogenous Inducing Factors, *Bioengineering*, 2023, **10**(12), 1438.

16 C. Chen, X. Bai, Y. Ding and I. S. Lee, Electrical stimulation as a novel tool for regulating cell behavior in tissue engineering, *Biomater. Res.*, 2019, **23**, 25.

17 J. S. Khaw, R. Xue, N. J. Cassidy and S. H. Cartmell, Electrical stimulation of titanium to promote stem cell orientation, elongation and osteogenesis, *Acta Biomater.*, 2022, **139**, 204–217.

18 P. Zarrintaj, B. Bakhshandeh, M. R. Saeb, F. Sefat, I. Rezaeian and M. R. Ganjali, *et al.*, Oligoaniline-based conductive biomaterials for tissue engineering, *Acta Biomater.*, 2018, **72**, 16–34.

594 | *Mol. Syst. Des. Eng.*, 2024, **9**, 581–596

This journal is © The Royal Society of Chemistry and IChemE 2024

19 P. Zarrintaj, B. Bakhshandeh, I. Rezaeian, B. Heshmatian and M. R. Ganjali, A novel electroactive agarose-aniline pentamer platform as a potential candidate for neural tissue engineering, *Sci. Rep.*, 2017, **7**(1), 1–12.

20 H. Kagami, H. Agata and A. Tojo, Bone marrow stromal cells (bone marrow-derived multipotent mesenchymal stromal cells) for bone tissue engineering: basic science to clinical translation, *Int. J. Biochem. Cell Biol.*, 2011, **43**(3), 286–289.

21 F. Shang, Y. Yu, S. Liu, L. Ming, Y. Zhang and Z. Zhou, *et al.*, Advancing application of mesenchymal stem cell-based bone tissue regeneration, *Bioact. Mater.*, 2021, **6**(3), 666–683.

22 A. Arthur and S. Gronthos, Clinical application of bone marrow mesenchymal stem/stromal cells to repair skeletal tissue, *Int. J. Mol. Sci.*, 2020, **21**(24), 9759.

23 J. K. Leach and J. Whitehead, Materials-directed differentiation of mesenchymal stem cells for tissue engineering and regeneration, *ACS Biomater. Sci. Eng.*, 2017, **4**(4), 1115–1127.

24 M. D. Griffin, T. Ritter and B. P. Mahon, Immunological aspects of allogeneic mesenchymal stem cell therapies, *Hum. Gene Ther.*, 2010, **21**(12), 1641–1655.

25 S. Mombini, J. Mohammadnejad, B. Bakhshandeh, A. Narmani, J. Nourmohammadi and S. Vahdat, *et al.*, Chitosan-PVA-CNT nanofibers as electrically conductive scaffolds for cardiovascular tissue engineering, *Int. J. Biol. Macromol.*, 2019, **140**, 278–287.

26 A. Abedi, B. Bakhshandeh, A. Babaie, J. Mohammadnejad, S. Vahdat and R. Mombeiny, *et al.*, Concurrent application of conductive biopolymeric chitosan/polyvinyl alcohol/ MWCNTs nanofibers, intracellular signaling manipulating molecules and electrical stimulation for more effective cardiac tissue engineering, *Mater. Chem. Phys.*, 2021, **258**, 123842.

27 G. P. Awasthi, V. K. Kaliannagounder, B. Maharjan, J. Y. Lee, C. H. Park and C. S. Kim, Albumin-induced exfoliation of molybdenum disulfide nanosheets incorporated polycaprolactone/zein composite nanofibers for bone tissue regeneration, *Mater. Sci. Eng., C*, 2020, **116**, 111162.

28 W. Z. Teo, E. L. Chng, Z. Sofer and M. Pumera, Cytotoxicity of exfoliated transition-metal dichalcogenides (MoS2 , WS2 , and WSe2 ) is lower than that of graphene and its analogues, *Chemistry*, 2014, **20**(31), 9627–9632.

29 H. Nazari, A. Heirani-Tabasi, E. Esmaeili, A. M. Kajbafzadeh, Z. Hassannejad and S. Boroomand, *et al.*, Decellularized human amniotic membrane reinforced by MoS2-Polycaprolactone nanofibers, a novel conductive scaffold for cardiac tissue engineering, *J. Biomater. Appl.*, 2022, **36**(9), 1527–1539.

30 S. Wang, K. Li, Y. Chen, H. Chen, M. Ma and J. Feng, *et al.*, Biocompatible PEGylated MoS2 nanosheets: controllable bottom-up synthesis and highly efficient photothermal regression of tumor, *Biomaterials*, 2015, **39**, 206–217.

31 I. S. Waskito, B. Kurniawan, M. I. Amal and M. Hanifuddin, The Effect of Precursors Concentration on the Structural Properties of MoS2 Nanosheet-Microsphere Synthesized Via Hydrothermal Route, *IOP Conf. Ser.: Mater. Sci. Eng.*, 2019, **546**(4), 042048.

32 Y. Ghiyasi, E. Salahi and H. Esfahani, Synergy effect of Urtica dioica and ZnO NPs on microstructure, antibacterial activity and cytotoxicity of electrospun PCL scaffold for wound dressing application, *Mater. Today Commun.*, 2021, **26**, 102163.

33 T. Kokubo and H. Takadama, How useful is SBF in predicting in vivo bone bioactivity?, *Biomaterials*, 2006, **27**(15), 2907–2915.

34 T. D. Schmittgen and K. J. Livak, Analyzing real-time PCR data by the comparative C(T) method, *Nat. Protoc.*, 2008, **3**(6), 1101–1108.

35 M. Yi and C. Zhang, The synthesis of MoS2 particles with different morphologies for tribological applications, *Tribol. Int.*, 2017, **116**, 285–294.

36 B. Balusamy, A. Celebioglu, A. Senthamizhan and T. Uyar, Progress in the design and development of "fast-dissolving" electrospun nanofibers based drug delivery systems-A systematic review, *J. Controlled Release*, 2020, **326**, 482–509.

37 C. Wang, W. Wang, L. Zhang, S. Zhong and D. Yu, Electrospinning of PAN/Ag NPs nanofiber membrane with antibacterial properties, *J. Mater. Res.*, 2019, **34**(10), 1669–1677.

38 H. Sadeghzadeh, A. Mehdipour, H. Dianat-Moghadam, R. Salehi, A. B. Khoshfetrat and A. Hassani, *et al.*, PCL/Col I-based magnetic nanocomposite scaffold provides an osteoinductive environment for ADSCs in osteogenic cues-free media conditions, *Stem Cell Res. Ther.*, 2022, **13**(1), 143.

39 D. T. Dixon and C. T. Gomillion, Conductive Scaffolds for Bone Tissue Engineering: Current State and Future Outlook, *J. Funct. Biomater.*, 2021, **13**(1), 1.

40 X. Zhang, T. Wang, Z. Zhang, H. Liu, L. Li and A. Wang, *et al.*, Electrical stimulation system based on electroactive biomaterials for bone tissue engineering, *Mater. Today*, 2023, 177–203.

41 A. Mirzaei, E. Saburi, S. E. Enderami, M. Barati Bagherabad, S. E. Enderami and M. Chokami, *et al.*, Synergistic effects of polyaniline and pulsed electromagnetic field to stem cells osteogenic differentiation on polyvinylidene fluoride scaffold, *Artif. Cells, Nanomed., Biotechnol.*, 2019, **47**(1), 3058–3066.

42 K. Dave and V. G. Gomes, Interactions at scaffold interfaces: Effect of surface chemistry, structural attributes and bioaffinity, *Mater. Sci. Eng., C*, 2019, **105**, 110078.

43 K. Ma, C. Liao, L. Huang, R. Liang, J. Zhao and L. Zheng, *et al.*, Electrospun PCL/MoS2 Nanofiber Membranes Combined with NIR-Triggered Photothermal Therapy to Accelerate Bone Regeneration, *Small*, 2021, **17**(51), 2104747.

44 S. Soliman, S. Sant, J. W. Nichol, M. Khabiry, E. Traversa and A. Khademhosseini, Controlling the porosity of fibrous scaffolds by modulating the fiber diameter and packing density, *J. Biomed. Mater. Res., Part A*, 2011, **96**(3), 566–574.

45 Y.-C. Chiu, H.-Y. Fang, T.-T. Hsu, C.-Y. Lin and M.-Y. Shie, The characteristics of mineral trioxide aggregate/ polycaprolactone 3-dimensional scaffold with osteogenesis properties for tissue regeneration, *J. Endod.*, 2017, **43**(6), 923–929.

46 H. Tohidlou, S. S. Shafiei, S. Abbasi, M. Asadi-Eydivand and M. Fathi-Roudsari, Amine-functionalized Single-walled Carbon Nanotube/Polycaprolactone Electrospun Scaffold for Bone Tissue Engineering: in vitro Study, *Fibers Polym.*, 2019, **20**(9), 1869–1882.

47 G. P. Awasthi, V. K. Kaliannagounder, B. Maharjan, J. Y. Lee, C. H. Park and C. S. Kim, Albumin-induced exfoliation of molybdenum disulfide nanosheets incorporated polycaprolactone/zein composite nanofibers for bone tissue regeneration, *Mater. Sci. Eng., C*, 2020, **116**, 111162.

48 C. Talayero, O. Aït-Salem, P. Gallego, A. Páez-Pavón, R. G. Merodio-Perea and I. Lado-Touriño, Computational prediction and experimental values of mechanical properties of carbon nanotube reinforced cement, *Nanomaterials*, 2021, **11**(11), 2997.

49 E. A. Chudinova, M. A. Surmeneva, A. S. Timin, T. E. Karpov, A. Wittmar and M. Ulbricht, *et al.*, Adhesion, proliferation, and osteogenic differentiation of human mesenchymal stem cells on additively manufactured Ti6Al4V alloy scaffolds modified with calcium phosphate nanoparticles, *Colloids Surf., B*, 2019, **176**, 130–139.

50 C. Jiang, K. Wang, X. Jiang, C. Zhang and B. Wang, Quantitative investigation of the process parameters of electrohydrodynamic direct-writing and their effects on fiber surface roughness and cell adhesion, *Polymer*, 2020, **12**(11), 2475.

51 R. Mahdavi, G. Belgheisi, M. Haghbin-Nazarpak, M. Omidi, A. Khojasteh and M. Solati-Hashjin, Bone tissue engineering gelatin-hydroxyapatite/graphene oxide scaffolds with the ability to release vitamin D: fabrication, characterization, and in vitro study, *J. Mater. Sci.: Mater. Med.*, 2020, **31**(11), 97.

52 L. Wang, M. Fang, Y. Xia, J. Hou, X. Nan and B. Zhao, *et al.*, Preparation and biological properties of silk fibroin/nano-hydroxyapatite/graphene oxide scaffolds with an oriented channel-like structure, *RSC Adv.*, 2020, **10**(17), 10118–10128.

53 F. S. Hosseini, F. Soleimanifar, A. Ardeshirylajimi, S. Vakilian, M. Mossahebi-Mohammadi and S. E. Enderami, *et al.*, In vitro osteogenic differentiation of stem cells with different sources on composite scaffold containing natural bioceramic and polycaprolactone, *Artif. Cells, Nanomed., Biotechnol.*, 2019, **47**(1), 300–307.

54 L. Leppik, K. M. C. Oliveira, M. B. Bhavsar and J. H. Barker, Electrical stimulation in bone tissue engineering treatments, *Eur. J. Trauma Emerg. Surg.*, 2020, **46**(2), 231–244.

55 M. Eischen-Loges, K. M. Oliveira, M. B. Bhavsar, J. H. Barker and L. Leppik, Pretreating mesenchymal stem cells with electrical stimulation causes sustained long-lasting pro-osteogenic effects, *PeerJ*, 2018, **6**, e4959.

56 P. S. Lee, C. Heinemann, K. Zheng, R. Appali, F. Alt and J. Krieghoff, *et al.*, The interplay of collagen/bioactive glass nanoparticle coatings and electrical stimulation regimes distinctly enhanced osteogenic differentiation of human mesenchymal stem cells, *Acta Biomater.*, 2022, **149**, 373–386.

57 J. M. Khalifeh, Z. Zohny, M. MacEwan, M. Stephen, W. Johnston and P. Gamble, *et al.*, Electrical Stimulation and Bone Healing: A Review of Current Technology and Clinical Applications, *IEEE Rev. Biomed. Eng.*, 2018, **11**, 217–232.

58 B. Bakhshandeh, N. Ranjbar, A. Abbasi, E. Amiri, A. Abedi and M. R. Mehrabi, *et al.*, Recent progress in the manipulation of biochemical and biophysical cues for engineering functional tissues, *Bioeng. Transl. Med.*, 2022, 1–29.

59 J. Zhu, Z. Qi, C. Zheng, P. Xue, C. Fu and S. Pan, *et al.*, Enhanced cell proliferation and osteogenesis differentiation through a combined treatment of poly-L-lysine-coated PLGA/graphene oxide hybrid fiber matrices and electrical stimulation, *J. Nanomater.*, 2020, **2020**, 1–15.

**596** | *Mol. Syst. Des. Eng.*, 2024, **9**, 581–596

This journal is © The Royal Society of Chemistry and IChemE 2024